Dipolar interaction induced band gaps and flat modes in surface-modulated magnonic crystals

Gallardo, R. A.; Schneider, T.; Roldan-Molina, A.; Langer, M.; Fassbender, J.; Lenz, K.; Lindner, J.; Landeros, P.;

Originally published:

April 2018

Physical Review B 97(2018), 144405

DOI: https://doi.org/10.1103/PhysRevB.97.144405

Dipolarly-induced band gaps and nearly flat modes in surface-modulated magnonic crystals

R. A. Gallardo,[1] T. Schneider,[2,3] A. Roldán-Molina,[4] M. Langer,[2,5]
J. Fassbender,[2] K. Lenz,[2] J. Lindner,[2] and P. Landeros[1]

[1] *Departamento de Física, Universidad Técnica Federico Santa María, Avenida España 1680, Valparaíso, Chile*
[2] *Helmholtz-Zentrum Dresden-Rossendorf, Instititute of Ion Beam Physics and Materials Research, Bautzner Landstr. 400, 01328 Dresden, Germany*
[3] *Department of Physics, Technische Universität Chemnitz, Reichenhainer Str. 70, 09126 Chemnitz, Germany*
[4] *Universidad de Aysén, Calle Obispo Vielmo 62, Coyhaique, Chile*
[5] *Institute for Physics of Solids, Technische Universität Dresden, Zellescher Weg 16, 01069 Dresden, Germany*

(Dated: September 12, 2017)

Theoretical results for the magnetization dynamics of surface-modulated magnonic crystals (SMMCs) are presented. For such systems, the role of the periodic dipolar field induced by the geometrical modulation is addressed by using the plane-wave method. The results unveil that under the increasing of the etched depth, zones with magnetizing and demagnetizing fields act on the system, in such a way that magnonic band gaps are observed in both Damon-Eshbach (DE) and backward volume (BV) geometries. Particularly, in BV configuration, high frequency band gaps and low frequency nearly flat modes are obtained. By controlling the geometry of the etched zones, the frequency modes, spatial profiles and forbidden frequency gaps of spin waves (SWs) can be manipulated. To test the validity of the model, the theoretical results of this work are confirmed by micromagnetic simulations, where a good agreement between both methods is achieved. It is demonstrated that the spin-wave dynamics of a surface modulated magnonic crystal contrasts to bi-component magnonic crystals or periodic arrays of wires, for instance, since the SMMCs allow enhancing the magnetizing character in some regions of the film, promoting thus the confinement of the SWs. The theoretical model allows for a detailed understanding of the physics underlying these kind of systems, thereby providing an outlook to potential applications on magnonic devices.

I. INTRODUCTION

Spin waves at microwave frequencies are of current potential interest for wireless communication technologies, since they can transport and handle information in a unique way.[1,2] Such waves are able to carry pure spin currents (currents without charge transport that can be converted into measurable charge currents), even in magnetic insulators.[3] One of the potential aspects of SW-based technologies is that both the amplitude and the phase of spin waves may encode information.[4,5] Besides, SWs have further been proposed as building blocks for computational architectures allowing to perform logic operations.[6–8] The manipulation of SW propagation by means of periodic modulation of magnetic or geometrical properties can be regarded as an important research field in magnetism.[9–17] Such research area is currently named magnonics or magnon-spintronics, and it is based on the control of SWs in periodic magnetic structures called magnonic crystals (MCs).[1,2,18] The possibility of such system to act as a SW filter with a pronounced discretization of the frequency turns out to be key for applications in signal processing and storage-recovery mechanisms.[15,19] In this context, MCs have been extensively studied, since they exhibit adjustable frequency band gaps (BGs), which can be optimized by modulating the magnetic parameters or changing the geometry and arrangement of periodic scattering centers.[9–17,19–34] The design of the MCs can be realized by artificial modulation of the magnetic properties, either in the form of dipolarly coupled nanowires[23], bi-component magnonic crystals,[12–14] width-modulated waveguides,[32,33] antidot lattices,[35,36] modulated thickness nanowires,[37–40] or by means of ion-implantation.[41–43] Also, reconfigurable magnonic crystals with periodically induction of perpendicular magnetic anisotropy have been designed.[44]

A large variety of studies based on Brillouin light scattering have been carried out on MCs,[11–14] where the presence of frequency band gaps has been confirmed in full accordance with theoretical results. Moreover, bi-component MCs have been widely studied,[12–14,45–47] where periodic properties originate from a different saturation magnetization M_s, anisotropy K, or exchange constant A. Thus, modification of these parameters allows for controlling the BG position and the localization of SWs. For instance, increasing the contrast of M_s of a bi-component MC can lead to a broadening of the BG frequency range and enable the concentration of a spin-wave excitation within the zone of lower or higher saturation magnetization. However, experimentally defining material parameters such as magnetization or exchange length with laterally well-defined periodicities often is not straightforward and suffering from limitations of the range in which variations are possible for a given material. A periodic surface modulation of a ferromagnetic (FM) thin film is an interesting alternative for creating magnonic structures and devices, where

the periodic properties are attributed to the size of the modulation. A surface-modulated magnonic crystal exhibits zones with demagnetizing and magnetizing characters. The demagnetizing field is acting in the thicker parts of the SMMC, which reduces the total internal field. On the other side, the magnetizing character of the field dominates in the trenches, in such a way that the dynamics of the SWs can be notoriously different, since such a magnetizing field increases the internal field that drives the motion of the spin waves. In a fully etched MC, there is no magnetizing field acting in the magnetic material. On the other side, in bi-component MCs the magnetizing/demagnetizing fields are competing so that both magnetic material create magnetic charges at the interfaces and hence, such fields are reduced in comparison to SMMCs. In this paper, including the dipolar fields created by the trenches, the role of the demagnetizing and magnetizing fields in the SMMC is theoretically discussed. It is shown that the periodic dipolar fields open frequency band gaps in both DE and BV configurations. Particularly, in BV geometry the strong contrast between the demagnetizing and magnetizing fields induces a high localization degree of the SW, which is almost independent of the wave vector, in such a way that nearly flat modes are obtained. By controlling the geometry of the etched zones, the mode frequencies, spatial profiles and forbidden frequency gaps of spin waves can be manipulated.

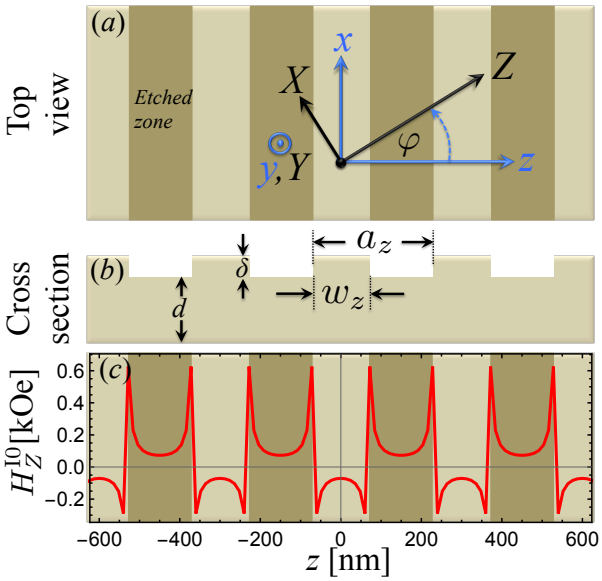

FIG. 1. In (a) the top view of the surface-modulated MC is shown, where two coordinate systems are depicted. The coordinates (x,y,z) are defined by the geometry periodic structure's geometry, while (X,Y,Z) is defined according to the equilibrium orientation of the magnetization, which points along Z, with X lying in the film's plane. In (b) the cross section is shown, where d denotes the thickness of the nominal film, δ is the thickness of the etched zones, a_z is the lattice parameter along z-direction and w_z is the width of the thicker part of the film. The red curve in figure (c) shows the periodic dipolar field [see Eqs. (7) and (8)] created by the static magnetic charges at the edges of the etched zones for $\delta = 2$ nm and $\varphi = 0$. Additional magnetic parameters are given in section III.

II. THEORETICAL DESCRIPTION

In bi-component magnonic crystals, the periodic properties originate from the contrast between different ferromagnetic materials with different magnetic parameters, for instance the saturation magnetization M_s or exchange constant A. Nevertheless in surface-modulated magnonic crystals the periodic properties arise from the magnetic charges created at the edges of the etched zones, as shown Fig. 1(b) for a one-dimensional surface-modulated magnonic crystal.

The temporal evolution of the system can be described using the Landau-Lifshitz (LL) equation $\dot{\mathbf{M}}(\mathbf{r};t) = -\gamma\mathbf{M}(\mathbf{r};t)\times\mathbf{H}^\mathrm{e}(\mathbf{r};t)$. Here, γ is the absolute value of the gyromagnetic ratio, $\mathbf{M}(\mathbf{r};t)$ is the magnetization and $\mathbf{H}^\mathrm{e}(\mathbf{r};t)$ is the effective field. For small deviations around the equilibrium, both the magnetization and the effective field are written as $\mathbf{M}(\mathbf{r};t) = M_\mathrm{s}\hat{Z} + \mathbf{m}(\mathbf{r};t)$ and $\mathbf{H}^\mathrm{e}(\mathbf{r};t) = \mathbf{H}^{\mathrm{e}0}(\mathbf{r}) + \mathbf{h}^\mathrm{e}(\mathbf{r};t)$, respectively. Note that $\hat{Z}$ points along the equilibrium orientation of the magnetization, which lies in-plane and $\mathbf{h}^\mathrm{e}(\mathbf{r};t)$ is proportional to the dynamic magnetization $\mathbf{m}(\mathbf{r};t)$. Thus, in the linear regime, the LL equation reads

$$i\Omega m_X(\mathbf{r}) = -m_Y(\mathbf{r})H_Z^{\mathrm{e}0}(\mathbf{r}) + M_\mathrm{s}h_Y^\mathrm{e}(\mathbf{r}) \quad (1a)$$
$$i\Omega m_Y(\mathbf{r}) = m_X(\mathbf{r})H_Z^{\mathrm{e}0}(\mathbf{r}) - M_\mathrm{s}h_X^\mathrm{e}(\mathbf{r}) \quad (1b)$$

wherein it has been assumed $\mathbf{h}^\mathrm{e}(\mathbf{r};t) = \mathbf{h}^\mathrm{e}(\mathbf{r})e^{i\omega t}$, and then $\mathbf{m}(\mathbf{r};t) = \mathbf{m}(\mathbf{r})e^{i\omega t}$, and it is also defined $\Omega = \omega/\gamma$. Moreover, note that $H_\eta^{\mathrm{e}0}$ (h_η^e) is the η-component of the static (dynamic) effective magnetic field. The effective field is defined as $\mathbf{H}^\mathrm{e}(\mathbf{r}) = \mathbf{H} + \mathbf{H}^\mathrm{ex}(\mathbf{r}) + \mathbf{H}^\mathrm{d}(\mathbf{r}) + \mathbf{H}^\mathrm{I}(\mathbf{r})$, where $\mathbf{H}$ is the external field, $\mathbf{H}^\mathrm{ex}(\mathbf{r}) = 4\pi\lambda_\mathrm{ex}^2\nabla^2\mathbf{M}(\mathbf{r})$ is the exchange field with $\lambda_\mathrm{ex}(\mathbf{r}) = 2A/4\pi M_\mathrm{s}$, wherein A is the exchange stiffness constant. Furthermore, $\mathbf{H}^\mathrm{d}(\mathbf{r})$ is the dipolar field of the flat film and $\mathbf{H}^\mathrm{I}(\mathbf{r})$ is the dipolar field induced by the periodic magnetic charges that reside at the edges of the etched zones $d < y < d+\delta$, where d is the thickness of the nominal film and δ is the etched depth (see Fig. 1). According to Fig. 1, the periodic distribution of the etched regions of thickness δ over the top surface of the ferromagnetic film induces a periodic stray field that interacts with the magnetization of the nominal film. In this way, according to Bloch's theorem, the dynamic components of the magnetization can be expanded into Fourier series as $\mathbf{m}(\mathbf{r}) = \sum_\mathbf{G}\mathbf{m}(\mathbf{G})e^{i(\mathbf{G}+\mathbf{k})\cdot\mathbf{r}}$, where $\mathbf{G} = G_q\hat{x} + G_n\hat{z}$ denotes a reciprocal lattice vector, with $G_q = (2\pi/a_x)q$, $G_n = (2\pi/a_z)n$ and both n and q are integer numbers. The above picture considers a general two-dimensional periodic modulation of the etched zones, which can be easily adapted to one-dimensional periodic

structures by setting $G_q = 0$, as depicted in Fig. 1. Thus, the dynamic components of the dipolar field averaged over the film's thickness are

$$h_Y^{\rm d}(\mathbf{r}) = -4\pi \sum_{\mathbf{G}} m_Y(\mathbf{G})\zeta(\mathbf{G}+\mathbf{k},d)e^{i(\mathbf{G}+\mathbf{k})\cdot\mathbf{r}} \quad (2)$$

and

$$h_X^{\rm d}(\mathbf{r}) = 4\pi \sum_{\mathbf{G}} m_X(\mathbf{G})\xi(\mathbf{G},\mathbf{k})^2 \frac{\zeta(\mathbf{G}+\mathbf{k},d)-1}{|\mathbf{G}+\mathbf{k}|^2} e^{i(\mathbf{G}+\mathbf{k})\cdot\mathbf{r}}, \quad (3)$$

where

$$\zeta(\mathbf{Q},d) = \frac{2\sinh[|\mathbf{Q}|d/2]e^{-|\mathbf{Q}|d/2}}{|\mathbf{Q}|d} \quad (4)$$

and

$$\xi(\mathbf{G},\mathbf{k}) = (G_n + k_z)\sin\varphi - (G_q + k_x)\cos\varphi. \quad (5)$$

Likewise, the exchange dynamic field components are

$$h_{X,Y}^{\rm ex}(\mathbf{r}) = -4\pi\lambda_{\rm ex}^2 \sum_{\mathbf{G}} (\mathbf{G}+\mathbf{k})^2 m_{X,Y}(\mathbf{G}) e^{i(\mathbf{G}+\mathbf{k})\cdot\mathbf{r}}. \quad (6)$$

The Z-component of the static dipolar field created by the edges of the etches zones can be written as $H_Z^{\rm I0}(\mathbf{r}) = H_{1Z}^{\rm I0}(\mathbf{r}) + H_{2Z}^{\rm I0}(\mathbf{r})$, with $H_{1Z}^{\rm I0}(\mathbf{r})$ $[H_{2Z}^{\rm I0}(\mathbf{r})]$ being the static field inside the zone $d > y > 0$ $(d+\delta > y > d)$. These components are (see details in appendix A)

$$H_{1Z}^{\rm I0}(\mathbf{r}) = -2\pi M_{\rm s} \sum_{\mathbf{G}} C_{\mathbf{G}}\chi(\mathbf{G})^2 \frac{\eta(\mathbf{G})d}{|\mathbf{G}|^2(d+\delta)} e^{i\mathbf{G}\cdot\mathbf{r}} \quad (7)$$

and

$$H_{2Z}^{\rm I0}(\mathbf{r}) = 4\pi M_{\rm s} \sum_{\mathbf{G}} C_{\mathbf{G}}\chi(\mathbf{G})^2 \delta \frac{\zeta(\mathbf{G},\delta)-1}{|\mathbf{G}|^2(d+\delta)} e^{i\mathbf{G}\cdot\mathbf{r}}. \quad (8)$$

where,

$$\eta(\mathbf{G}) = \frac{e^{-|\mathbf{G}|(d+\delta)}}{|\mathbf{G}|d}(e^{|\mathbf{G}|d}-1)(e^{|\mathbf{G}|\delta}-1). \quad (9)$$

Also, the dynamic components of the magnetization are

$$h_Y^{\rm I}(\mathbf{r}) = 2\pi \sum_{\mathbf{G},\mathbf{G}'} C_{\mathbf{G}'} e^{i(\mathbf{G}+\mathbf{G}'+\mathbf{k})\cdot\mathbf{r}} \{m_Y(\mathbf{G})\eta(\mathbf{G}+\mathbf{G}'+\mathbf{k}) - im_X(\mathbf{G})\xi(\mathbf{G}+\mathbf{G}',\mathbf{k})\frac{\eta(\mathbf{G}+\mathbf{G}'+\mathbf{k})}{|\mathbf{G}+\mathbf{G}'+\mathbf{k}|}\}, \quad (10)$$

and

$$h_X^{\rm I}(\mathbf{r}) = -2\pi \sum_{\mathbf{G},\mathbf{G}'} C_{\mathbf{G}'} e^{i(\mathbf{G}+\mathbf{G}'+\mathbf{k})\cdot\mathbf{r}} \times \left\{ m_X(\mathbf{G})\xi(\mathbf{G}+\mathbf{G}',\mathbf{k})^2 \frac{\eta(\mathbf{G}+\mathbf{G}'+\mathbf{k})}{|\mathbf{G}+\mathbf{G}'+\mathbf{k}|^2} + im_Y(\mathbf{G})\xi(\mathbf{G}+\mathbf{G}',\mathbf{k})\frac{\eta(\mathbf{G}+\mathbf{G}'+\mathbf{k})}{|\mathbf{G}+\mathbf{G}'+\mathbf{k}|}\right\}. \quad (11)$$

In Eqs. (7), (8), (10) and (11) the coefficients $C_{\mathbf{G}}$ accounts the geometry of the periodic structure, which may be in the form of stripes, circular dots, squares, etc.[43] In general, the static field component $H_Z^{\rm I0}(\mathbf{r})$ and the dynamic one $h_{X,Y}^{\rm I}$ enter directly in the dynamics of the system through Eq. (1), while the $H_X^{\rm I0}(\mathbf{r})$ and $H_Y^{\rm I0}(\mathbf{r})$ components only affect the static properties of the system. Now, inserting all field contributions into Eq. (1), the following eigenvalue problem is obtained:

$$\tilde{\mathbf{A}}\ \mathbf{m}_{\mathbf{G}}^{\rm T} = i\Omega\ \mathbf{m}_{\mathbf{G}}^{\rm T} \quad (12)$$

where $\mathbf{m}_{\mathbf{G}}^{\rm T} = [m_X(G_1),...,m_X(G_N),m_Y(G_1),...,m_Y(G_N)]$ is the eigenvector and $\tilde{\mathbf{A}}$ is given by

$$\tilde{\mathbf{A}} = \begin{pmatrix} \tilde{\mathbf{A}}^{XX} & \tilde{\mathbf{A}}^{XY} \\ \tilde{\mathbf{A}}^{YX} & \tilde{\mathbf{A}}^{YY} \end{pmatrix}. \quad (13)$$

Explicit expressions of matrix elements of Eq. (13) can be find in App. B. Now, by using standard numerical methods and a convergence test to check the reliability of the results, the eigenvalues and eigenvectors of Eq. (12) can be obtained.

Additionally, to get insight into both the frequency-dependence of the modes and the SW profiles in the long wavelength limit, micromagnetic simulations have been carried out using the *MuMax*^{3} code.[48] Here, a magnetic film was built up in the (64; y; 4096) cells with the total dimensions of (256 nm; Y_c; 5.3 μm) with a mesh size of (4.0 nm; Y_c; 3.74 nm). Next, a 140 nm wide wire with thicknesses of (1 - 5 nm) was centrally put on top of the film, forming the intact film part. The wire was repeated 51 times with a spacing of a_z = 300 nm. To consider the reality of an extended surface modulated film, periodic boundary conditions were chosen along the x- and z-directions. The number of y-cells and the corresponding cell size Y_c was chosen according to the ratio of the wire thickness and the film thickness. The external field was applied in the z-direction, whereas the excitation field was chosen in y-direction. Two different kinds of simulations were carried out using the system described above. First, the spin wave dispersion relation was calculated similarly to the approach presented in Ref. 49, but the homogeneous excitation field was replaced by a localized rf field of approx. 140 nm width. The spin-wave dispersion was extracted using a spatial fast Fourier transform (FFT) approach along the z-direction. Furthermore, FMR simulations based on the approach given in Ref. 50 were carried out. The dynamic magnetization $\mathbf{m}(\mathbf{r},\omega)$ was extracted by employing a FFT in time for all cells. To obtain the SW profiles for a given frequency f_0 the transformed amplitude and phase was filtered and than transformed back into real space. Especially in the backward volume geometry this approach is very useful in the here presented system due to the more or less dispersionless spin wave branches. In Fig. 2(a) it is clearly visible that the main intensity is located in this dispersionless branches, making the analysis of higher order spin waves complicated. In the FMR approach this issue is

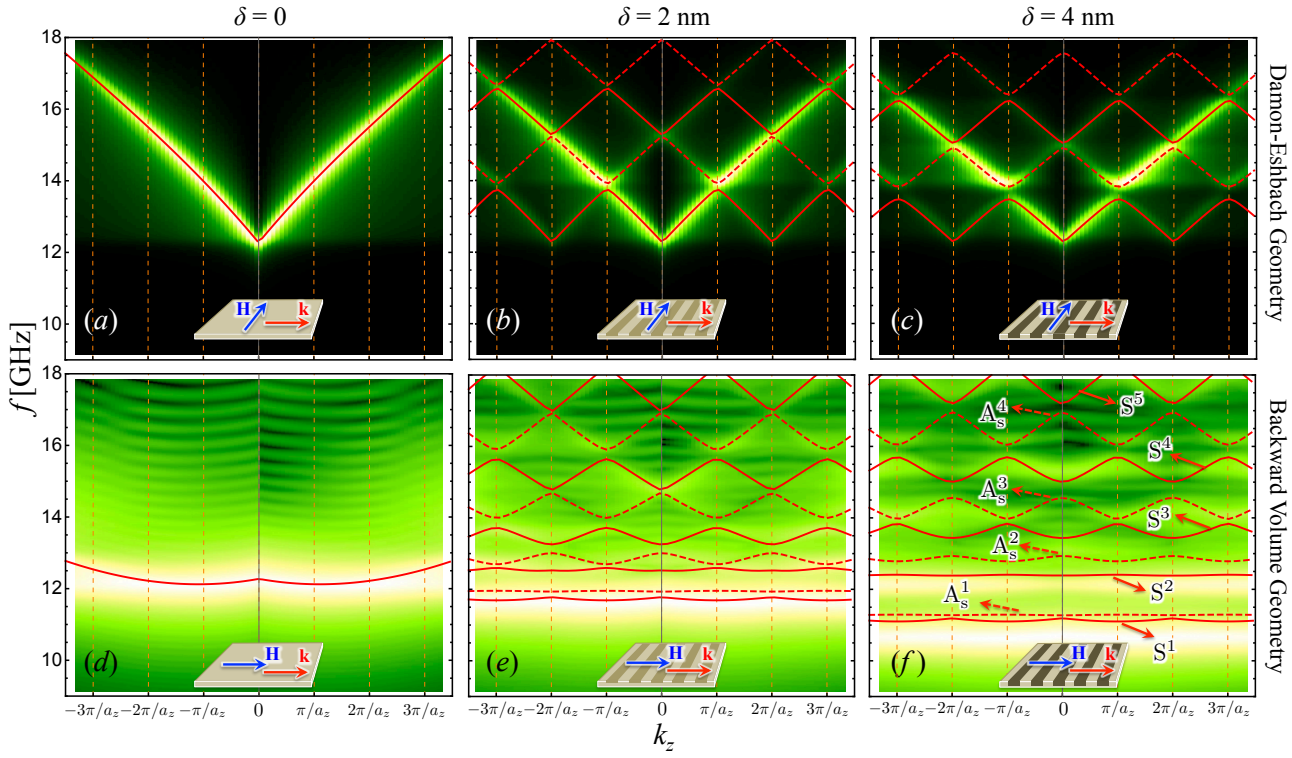

FIG. 2. (a), (b) and (c) show the dispersion relation in the DE geometry for $H = 1.5$ kOe and $\delta = 0$, 2 and 4 nm, respectively. Figs. (d), (e) and (f) depict the dispersion in BV configuration. The lines correspond to the theoretical results, while the micromagnetic simulations are represented by the code of colors, where the lighter (darker) color means to a maximum (minimum) of the response intensity. The modes have been labeled as S^{ν} and $\mathrm{A}_{\mathrm{s}}^{\nu}$ with $\nu = 1, 2, 3...$ The label S^{ν} ($\mathrm{A}_{\mathrm{s}}^{\nu}$) is defined according to the symmetric (antisymmetric) character of the spin-wave profiles around $z = 0$ at $k_z = 0$. In insets, the increasing of depth δ is represented as a darker color in the etched zones. In Figs. (d)–(f), the micromagnetic simulations are shown in log scale due to the dispersionless nature of the spin waves in the BV geometry, therefore a lighter background color is obtained.

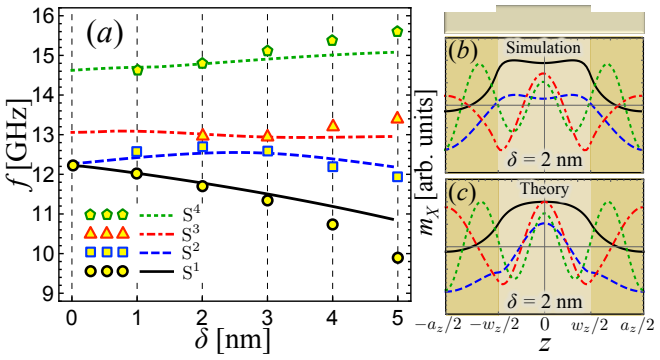

FIG. 3. In (a), the BV modes at $k_z = 0$ are shown as a function of δ. The lines (dots) represent the theoretical (simulated) calculations. In (b) and (c) the spin-wave profiles calculated by the simulations and theoretical model are depicted, respectively. In (a)–(c), the symmetric modes S^1, S^2, S^3 and S^4 are represented by solid, dashed, dot-dashed and dotted lines, respectively.

solved due to the fact that only $k_z = 0$ modes are excited. For the field–frequency dependence shown in Fig. 5 this approach was repeated for magnetic fields from 0 Oe to 2 kOe in 10 Oe steps. For this the FFT of the average magnetization component was considered. The magnetic parameters are the same used in the analytical approach, with a damping constant $\alpha = 10^{-2}$.

III. RESULTS AND DISCUSSION

The theoretical model will be applied now to thin films with one-dimensional stripe-like modulations, as shown in Fig. 1. For such geometry, the Fourier coefficients are given by by $C_{G_n} = (w_z/a_z)\mathrm{sinc}[(w_z/a_z)\pi n]$. Also, at 50 reciprocal lattice vectors, a convergence of the numerical solutions of Eq. (12) is reached. Typical permalloy parameters are used, namely a saturation magnetization $M_{\mathrm{s}} = 797$ emu/cm^3, stiffness constant $\lambda_{\mathrm{ex}} = 4.96$ nm and gyromagnetic ratio $\gamma = 0.0185556$ GHz/G. The geometrical parameters of the etched zones are $d + \delta = 10$ nm, $a_z = 300$ nm and $w_z = 140$ nm. Unless otherwise stated, the external field is $H = 1.5$ kOe. Note that these parameters have been chosen in concordance with the micromagnetic simulations.

In Fig. 2, the spin-wave dispersion relations are depicted in both Damon-Eshbach and backward volume ge-

ometries, when the depth δ of the surface modulation is varied. The color code visualizes the micromagnetic simulations, while the lines are obtained from the theoretical model. In Figs. 2(a), (b) and (c), dispersion relations in DE geometry ($\varphi = \pi/2$) are shown for δ =0, 2 and 4 nm, respectively. Here, it is clearly visible that the periodic stray fields created by the dynamic magnetic charges [see Eqs. (10) and (11)] open frequency BGs, whose strength can be controlled through the depth δ. On the other side, in Figs. 2(d)–(f) the BV spin waves are shown. Unlike the results of DE geometry, the SWs present a slightly dispersive branch at $\delta = 0$. Then, by increasing δ low frequency dispersionless modes are observed, while the high frequency ones have a clear periodic dispersion. In the simulations, the modes S^ν, which have symmetric character at $k_z = 0$, have strong intensities [see Figs. 3(b) and 3(c)], which can be modified by means of the external pulse included in the micromagnetic simulations. Due to the dispersionless property of the low frequency branches, the localization degree of the modes is practically independent of the wave vector. This is an important characteristic, because for conventional FMR measurements, most of the time, the detection is restricted on the symmetric modes only. Thus, this dynamic behavior of the spin waves in the BV geometry supports the usage of FMR techniques in periodic structures, like the ones created by ion irradiation.[41,43] Note that for $\delta > 4$ nm in Fig. 2(f) some deviations between simulations and calculations can be noticed. These deviations are attributed to the non-uniform distribution of the dynamic magnetization along the thickness. While δ increases the pinning conditions in the etched zones become important and therefore **m** varies along the normal axis y. Because this modulation is not considered in the theoretical model, some deviations between both methods are expected as δ increases. TOBIAS: Please include a comment about the modes in the background in the simulations in BV geometry

Fig. 3(a) shows the evolution of the first four modes S^1, S^2, S^3 and S^4 as a function of δ at $k_z = 0$. Here, it is observed that the theoretical model (lines) match very well with the numerical simulations (dots) in the range of $\delta \rightarrow 0 - 3$ nm. For higher depths, small deviations between theory and simulations are appreciated, as was explained before. The simulated and calculated dynamic magnetization profiles of m_X at $\delta = 2$ nm are illustrated in Figs. 3(b) and 3(c), respectively. Here, there is qualitatively good agreement between both methods, corroborating thus the approximations used in the theoretical model. The localization features of these standing spin waves depicted are almost independent of the wave vector, i.e., the SW profiles do not change at higher values of the wave vector (not shown). Also, this localization is strongly dependent of the stray field distribution, since the periodic dipole field is acting as demagnetizing field for the local magnetization in the thicker part. Therefore, at a fixed applied field the internal field in the thick part decreases the effective field, such that the mode is shifted

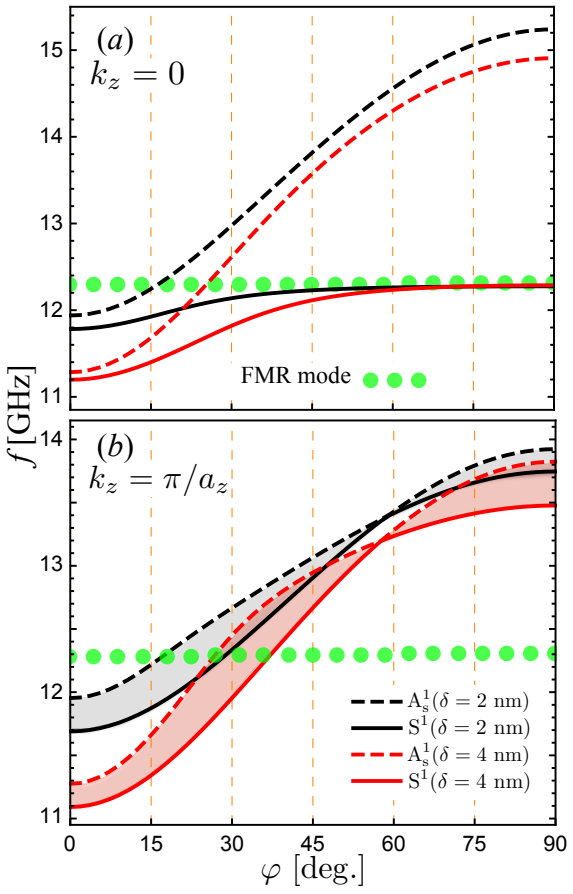

FIG. 4. Figures (a) and (b) show the angular dependence of the modes S^1 and A_s^1 evaluated at $k_z = 0$ and $k_z = \pi/a_z$, respectively. The cases $\delta = 2$ nm and 4 nm are depicted. The FMR mode ($k_z = 0$) of the perfect FM film ($\delta = 0$) is represented by filled circles. In (b) the shaded zones correspond to band-gap widths.

to lower frequencies.[40] The opposite behavior is observed in the thin part of the film, where he periodic dipole field is acting as a magnetizing field, and then the dipole field in the thin part increases the effective field. Thus, band gaps are opened by the dynamic dipole fields created by the dynamic magnetizations in DE configuration, where the BG width can be controlled via variation of δ, since at higher δ the dipolar field induced by dynamic magnetic charges becomes higher as well. On the other side, in backward volume configuration the high frequency BGs and the nearly flat modes are mainly induced by static magnetic charges. Because these static magnetic charges are induced by the static magnetization (perpendicular to the stripe-like modulations), they have an appreciable effect on the SW dynamics, i.e. the SWs are practically confined to some regions of the SMMC, as shown Figs. 3(b) and 3(c).

The evolution of the SWs between DE ($\varphi = 90°$) and BV ($\varphi = 0°$) configurations is shown in Fig. 4. Here, the first band gap (frequency difference of modes S^1 and A_s^1 at $k_z = \pi/a_z$) and modes at $k_z = 0$ are explored as a

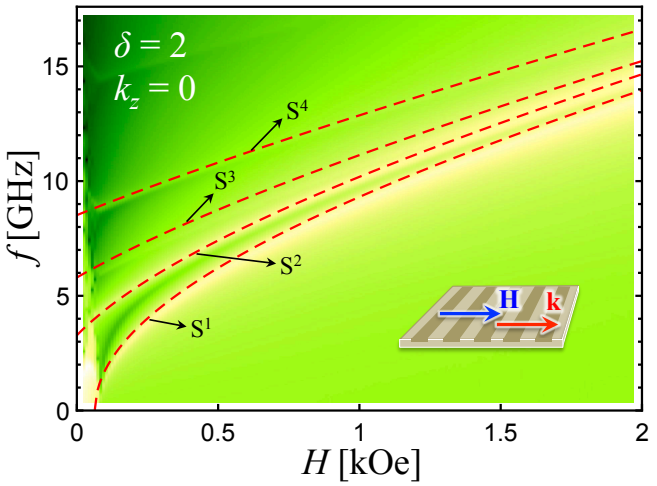

FIG. 5. Frequency as a function of the field for $\delta = 2$ nm and $k_z = 0$. The color code represent the simulated data, where the lighter (darker) color means to a maximum (minimum) of the response intensity. The lines correspond to the theoretical results for the first four symmetric modes.

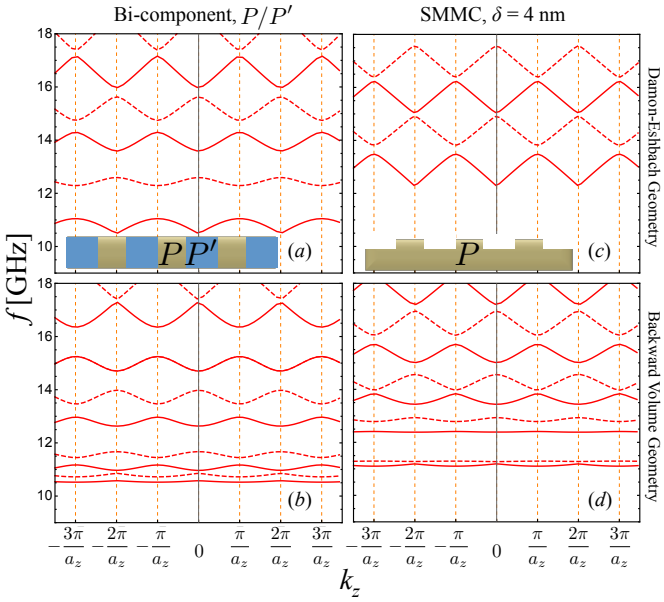

FIG. 6. (a) and (b) show the dispersion relation of the bi-component magnonic crystal composed by alternating P/P' magnetic materials in DE and BV geometries, respectively. A saturation magnetization M_s ($M'_s = 0.6M_s$) is used for P (P'). Figures (c) and (d) represent the SW dispersion for a SMMC.

function of the azimuthal angle φ. The filled circles represent the frequency position of the FMR mode of the perfect FM film (mode at $k_z = 0$ and $\delta = 0$), which is independent of the in-plane angle φ. In Fig. 4(a), one can see that near to the DE geometry ($\varphi = 90°$), the low frequency mode S^1, which dominates in intensity, is almost constant. However, when the angle φ is close to zero (BV spin waves) the S^1 mode moves to lower frequencies. This behavior can be understood by looking Fig. 4(b), since when the first band-gap [represented by the shaded zones in Fig. 4(b)] is close to the FMR mode (filled circles), this mode lies in the range of forbidden frequencies, and therefore it avoids this state and shifts to lower frequencies. In the FMR frequency vs. field diagram it is seen as a splitting of the spin-wave modes.[43] Thus, this effect is predominant in BV geometry, while in DE the gaps are opened at frequencies higher than the FMR mode and therefore the frequency position of the low frequency uniform mode does not change [see the low frequency FMR mode in Figs. 2(a)–(c)]. Figure 5 shows a comparison between theory and numerical simulations of the FMR response, where the evolution of the modes as a function of the field H is shown. The simulated calculations are given by the color code, whereas dashed lines represent the theoretical results.. Here, only the first four S^1, S^2, S^3 and S^4 modes are depicted, since from simulations point of view the excitation of antisymmetric modes requires an inhomogeneous excitation, which is not included in the micromagnetic code. Such behavior was previously obtained by using linear response theory and two-magnon scattering in the limit of perturbative modulation depths,[37,43] but restricted to the $k_z = 0$ limit.

The nearly flat modes obtained in the backward volume geometry for the 300 nm periodicity, whose SW localization is practically independent of the wave vector, represent a notorious impact in the SW dynamics. This effect is attributed to the enhancement of the magnetizing character in the thinner part of the film, in such a way that both demagnetizing and magnetizing fields induce confinement of the SW modes. In a fully etched MC ($\delta = d$), the magnetizing field lies in zones without magnetic material, and therefore it is not relevant for the dynamic properties of the SWs. On the other side, in bi-component MCs the magnetizing/demagnetizing fields are superimposed each other, because both magnetic materials create magnetic charges at the interfaces and thus, such fields are reduced in comparison to SMMCs. Figures 6(a) and (b) show the SW spectrum for a bi-component MC (see appendix C for details), while Figs. 6(c) and (d) illustrate the spectrum for a SMMC. For magnetic material P', a reduced saturation magnetization of $M'_s = 0.6(797)$ kA/m^2 was considered, while material P corresponds to the one previously described. From this figure, one can see that the bi-component system clearly presents BG widths larger than the SMMCs in both DE and BV geometries. Nevertheless, in Figs. 6(a) and (b) it easy to see that the low-frequency mode at $k_z = 0$ remains in the same frequency position (around 10.5 GHz) in both BV and DE configurations. A similar behavior is observed in typical one-dimensional MCs composed by alternating Permalloy/Cobalt stripes (not shown). This dynamic behavior in a bi-component MC is clearly different in the etched sample, where the low-frequency mode at $k_z = 0$ moves to lower frequencies in the BV geometry (around 12.5 GHz in DE and 11 GHz in

BV for $\delta = 4$ nm). At the same time, the modes having higher frequencies also mimic this behavior, namely they move to low frequencies and become nearly flat.

All the calculations presented in Sec. II show symmetric dispersion under the inversion of the wave vector, despite the fact that the elements $\mathbf{A}^{XX}_{\mathbf{G},\mathbf{G}'}$ and $\mathbf{A}^{YY}_{\mathbf{G},\mathbf{G}'}$ [see Eq. (B1a)] are dependent of the sign of the wave vector through function $\xi(\mathbf{G},\mathbf{k})$, defined in Eq. (5). Therefore, two counterpropagating SWs exhibit a full frequency reciprocity, namely $f(\mathbf{k}) = f(-\mathbf{k})$. This is not surprising, since if $\mathbf{A}^{XX}_{\mathbf{G},\mathbf{G}'} = -\mathbf{A}^{YY}_{\mathbf{G},\mathbf{G}'}$, the dispersion relation of spin waves depends on the square of $\xi(\mathbf{G},\mathbf{k})$. Nevertheless, if the dynamic components of the magnetization vary along the thickness, such as for the so-called first perpendicular standing SW mode, for instance; the SW frequency becomes dependent on the wave vector orientation and non-reciprocal features appear, i.e. $f(\mathbf{k}) \neq f(-\mathbf{k})$, since the condition $\mathbf{A}^{XX}_{\mathbf{G},\mathbf{G}'} = -\mathbf{A}^{YY}_{\mathbf{G},\mathbf{G}'}$ is broken. This effect has been observed in Refs. 51 and 52 for FM films with different magnetic (or geometrical) properties on top and bottom surfaces, where basically the symmetry is broken along the thickness by introducing different magnetic anisotropies at the surfaces[51] and by considering antiferromagnetic states between the magnetization in the etched zones ($d + \delta < y < d$) and the underneath FM film of thickness d.[52] Note that in the one-dimensional case $\xi(\mathbf{G},\mathbf{k}) = (G_n + k_z)\sin\varphi$, and therefore the non-reciprocal properties could be enhanced in the Damon-Eshbach geometry ($\varphi = 90°$), such as the case of spin waves propagating in FM/heavy-metal alloys, where the Dzyaloshinskii-Moriya interaction is important.[53–58]

IV. CONCLUSIONS

Spin waves in surface-modulated magnonic crystals were theoretically modeled using the plane-wave method and micromagnetic simulations. The theory shows that the dipolar interaction produced by surface geometrical modulation is capable to open magnonic band gaps either in the backward volume or Damon-Eshbach configurations, whose magnitude can be controlled by the etching height. An interesting evolution of the modes is founded in the backward volume configuration, where low frequency dispersionless modes are obtained, whose localization is almost independent of the wave vector. Such nearly flat magnonic bands are induced by the notable field contrast between magnetizing and demagnetizing regions of the SMMC. The theoretical results show that partially-etched ferromagnetic structures can serve as a interesting magnonic device capable of manipulating the spin wave properties, such as, band gaps, spin-wave localization, dispersionless modes, etc. by means of the etching depth; in contrast to the typical existing models for bi-component magnonic crystals, where the magnetic contrast between the constituent magnetic materials is along the entire thickness of the film. The approach agrees very well with numerical simulations, which allows validating the theoretical findings. Consequently, the model applied to periodically etched films provides further key-information about band gaps modulation, spatial localization of the modes and the dispersion of the spin waves. Therefore, the results obtained in this work offer a better understanding of such systems paving the way for further developments on MC-based devices.

Authors acknowledge financial support from CONICYT PAI/ACADEMIA 79140033, CONICYT/DAAD PCCI140051, FONDECYT 1161403, and Centers of excellence with Basal/CONICYT financing, grant FB0807, CEDENNA. Funding from Deutsche Forschungsgemeinschaft (grants no. LE2443/5-1 and GE1202/9-2) and DAAD PPP ALECHILE (grant no. 57136331) is highly acknowledged. T. S. acknowledges funding from the InProTUC scholarship.

Appendix A: Dipolar field induced by the etched zones

In order to obtain the static periodic field $\mathbf{H}^{\mathrm{I0}}(\mathbf{r})$, it is noted that the static magnetization components in the range $d < y < d + \delta$, can be written as

$$M_z = M_\mathrm{s}\cos\varphi \sum_{\mathbf{G}} C_{\mathbf{G}} \exp\left[i\mathbf{G}\cdot\mathbf{r}\right] \tag{A1}$$

and

$$M_x = M_\mathrm{s}\sin\varphi \sum_{\mathbf{G}} C_{\mathbf{G}} \exp\left[i\mathbf{G}\cdot\mathbf{r}\right]. \tag{A2}$$

Then, following Ref. 43, the magnetostatic potential is given by

$$\phi(\mathbf{r}) = -iM_\mathrm{s}\sum_{\mathbf{G}}\chi(\mathbf{G})\int C_{\mathbf{G}}\frac{e^{i\mathbf{G}\cdot\mathbf{r}'}}{|\mathbf{r}-\mathbf{r}'|}\mathrm{d}^3\mathbf{r}', \tag{A3}$$

where $\chi(\mathbf{G}) = G_n\cos\varphi + G_q\sin\varphi$. Besides, $C_{\mathbf{G}}$ is the Fourier coefficient that is not zero for $d + \delta > y' > d$ and zero otherwise. Therefore, an analytical expression can be derived for the magnetostatic potential, which is $\phi(\mathbf{r}) = \phi_1(\mathbf{r}) + \phi_2(\mathbf{r})$, where

$$\phi_1(\mathbf{r}) = i2\pi M_\mathrm{s}\sum_{\mathbf{G}} C_{\mathbf{G}}\chi(\mathbf{G})\frac{e^{|\mathbf{G}|(y-d-\delta)}\left(1-e^{|\mathbf{G}|\delta}\right)}{|\mathbf{G}|^2}e^{i\mathbf{G}\cdot\mathbf{r}}$$

and

$$\phi_2(\mathbf{r}) = i4\pi M_\mathrm{s}\sum_{\mathbf{G}} C_{\mathbf{G}}\chi(\mathbf{G})\times \frac{1-\cosh\left[|\mathbf{G}|(d+\delta/2-y)\right]e^{|\mathbf{G}|\delta/2}}{|\mathbf{G}|^2}e^{i\mathbf{G}\cdot\mathbf{r}}.$$

Here, function for $\phi_1(\mathbf{r})$ is the magnetic potential in the range $0 < y < d$, while $\phi_2(\mathbf{r})$ belongs to the range $d < y < d+\delta$. Thus, the Z-component of the static magnetic

field is $H_Z^{\mathrm{I0}}(\mathbf{r}) = H_{1Z}^{\mathrm{I0}}(\mathbf{r}) + H_{2Z}^{\mathrm{I0}}(\mathbf{r})$, with $H_{1Z}^{\mathrm{I0}}(\mathbf{r})$ $[H_{2Z}^{\mathrm{I0}}(\mathbf{r})]$ being the static field inside the zone $d > y > 0$ $(d+\delta > y > d)$. Then, the field can be obtained from $\mathbf{H}_1^{\mathrm{I0}}(\mathbf{r}) = -\nabla_{\mathbf{r}}\phi_1$ and $\mathbf{H}_2^{\mathrm{I0}}(\mathbf{r}) = -\nabla_{\mathbf{r}}\phi_2$, whose Z-components are given in Eqs. (7) and (8)

In expressions (7) and (8), an average over the thickness $d+\delta$ has been performed. Note that the magnetic field $H_{1Z}^{\mathrm{I0}}(\mathbf{r})$ dominates when the thickness of the etched zone is small, nevertheless when δ increases the field $H_{2Z}^{\mathrm{I0}}(\mathbf{r})$ becomes important. Thus, it is expected to reproduce surface-modulated magnonic crystals with significant depths. On the other hand, the dynamic magnetization components in the etched part can be written as

$$m_{X,Y}(\mathbf{r}) = \sum_{\mathbf{G},\mathbf{G}'} m_{X,Y}(\mathbf{G}) C_{\mathbf{G}'} e^{i(\mathbf{G}+\mathbf{G}'+\mathbf{k})\cdot\mathbf{r}}, \quad \text{(A4)}$$

where it is assumed that this dynamic magnetization is uniform along the thickness. This approximation is valid for small values of depth δ, nevertheless, when δ increases the boundary conditions may produce a modulation of spin waves along the thickness and therefore Eq. (A4) is not valid anymore. By using the same procedure to derive Eqs. (7) and (8), the dynamic components of shown in Eqs. (10) and (11) are obtained.

Appendix B: Matrix elements for a SMMC

The matrix elements in Eq. (13) are given by

$$\mathbf{A}^{XX}_{\mathbf{G},\mathbf{G}'} = -\mathbf{A}^{YY}_{\mathbf{G},\mathbf{G}'} = -i2\pi M_{\mathrm{s}} C_{\mathbf{G}-\mathbf{G}'} \xi(\mathbf{G},\mathbf{k}) \frac{\eta(\mathbf{G}+\mathbf{k})}{|\mathbf{G}+\mathbf{k}|}, \quad \text{(B1a)}$$

$$\mathbf{A}^{XY}_{\mathbf{G},\mathbf{G}'} = -\left[4\pi M_{\mathrm{s}}\lambda_{\mathrm{ex}}^2(\mathbf{G}+\mathbf{k})^2 + 4\pi M_{\mathrm{s}}\zeta(\mathbf{G}+\mathbf{k},d) + H\right]\delta_{\mathbf{G},\mathbf{G}'} + 2\pi M_{\mathrm{s}} C_{\mathbf{G}-\mathbf{G}'} F^{\mathrm{I}}_{XY} + \Psi(\mathbf{G}',\mathbf{G}), \quad \text{(B1b)}$$

$$\mathbf{A}^{YX}_{\mathbf{G},\mathbf{G}'} = \left[4\pi M_{\mathrm{s}}\lambda_{\mathrm{ex}}^2(\mathbf{G}+\mathbf{k})^2 + 4\pi M_{\mathrm{s}}\xi(\mathbf{G},\mathbf{k})^2 \frac{1-\zeta(\mathbf{G}+\mathbf{k},d)}{|\mathbf{G}+\mathbf{k}|^2} + H\right]\delta_{\mathbf{G},\mathbf{G}'} + 2\pi M_{\mathrm{s}} C_{\mathbf{G}-\mathbf{G}'} F^{\mathrm{I}}_{YX} - \Psi(\mathbf{G}',\mathbf{G}). \quad \text{(B1c)}$$

Here, it has been assumed that the external field is strong enough to orient the magnetization parallel to it. Also, functions F^{I}_{XY} and F^{I}_{YX} come from the dipolar interaction between the etched zone and the thick part and are given by

$$F^{\mathrm{I}}_{XY} = \eta(\mathbf{G}+\mathbf{k}) + \frac{\chi(\mathbf{G}-\mathbf{G}')^2}{|\mathbf{G}-\mathbf{G}'|^2} \frac{\eta(\mathbf{G}-\mathbf{G}')d}{d+\delta} \quad \text{(B2)}$$

and

$$F^{\mathrm{I}}_{YX} = \xi(\mathbf{G},\mathbf{k})^2 \frac{\eta(\mathbf{G}+\mathbf{k})}{|\mathbf{G}+\mathbf{k}|^2} - \frac{\chi(\mathbf{G}-\mathbf{G}')^2}{|\mathbf{G}-\mathbf{G}'|^2} \frac{\eta(\mathbf{G}-\mathbf{G}')d}{d+\delta}. \quad \text{(B3)}$$

While function $\Psi_{\mathbf{G}',\mathbf{G}}$ comes from the static stray field $H_{2Z}^{\mathrm{I0}}(\mathbf{r})$ that is interacting in the etched zone. This function is

$$\Psi(\mathbf{G}',\mathbf{G}) = \frac{4\pi M_{\mathrm{s}}\delta}{d+\delta} \sum_{\mathbf{G}''} C_{\mathbf{G}''-\mathbf{G}'} C_{\mathbf{G}-\mathbf{G}''} \times \frac{\chi(\mathbf{G}''-\mathbf{G}')^2}{|\mathbf{G}''-\mathbf{G}'|^2} \left[1-\zeta(\mathbf{G}''-\mathbf{G}',\delta)\right]. \quad \text{(B4)}$$

Appendix C: Matrix elements for a bi-component MC

In the case of a bi-component magnonic crystal depicted in Fig. 6, both the saturation magnetization and the exchange length are periodic functions. If the saturation magnetization changes from M_{s} to M'_{s}, then it can be written as

$$M_{\mathrm{s}}(\mathbf{r}) = \sum_{\mathbf{G}} M_{\mathrm{s}}(\mathbf{G}) e^{i\mathbf{G}\cdot\mathbf{r}}. \quad \text{(C1)}$$

In the same way, the exchange length is

$$\lambda_{\mathrm{ex}}(\mathbf{r}) = \sum_{\mathbf{G}} \lambda_{\mathrm{ex}}(\mathbf{G}) e^{i\mathbf{G}\cdot\mathbf{r}}, \quad \text{(C2)}$$

since $\lambda_{\mathrm{ex}}(\mathbf{r}) = 2A/4\pi M_{\mathrm{s}}$. Then, the matrix elements on Eq. (13) are given by $\mathbf{A}^{XX}_{\mathbf{G},\mathbf{G}'} = \mathbf{A}^{YY}_{\mathbf{G},\mathbf{G}'} = 0$,

$$\mathbf{A}^{XY}_{\mathbf{G},\mathbf{G}'} = -H\delta_{\mathbf{G},\mathbf{G}'} + 4\pi M_{\rm s}(\mathbf{G}-\mathbf{G}')\left[\chi(\mathbf{G}-\mathbf{G}')^2\frac{1-\zeta(\mathbf{G}-\mathbf{G}',d)}{|\mathbf{G}-\mathbf{G}'|^2} - \zeta(\mathbf{G}'+\mathbf{k},d)\right]$$
$$- 4\pi\sum_{\mathbf{G}''} M_{\rm s}(\mathbf{G}-\mathbf{G}'')\left[(\mathbf{G}'+\mathbf{k})\cdot(\mathbf{G}''+\mathbf{k}) - (\mathbf{G}-\mathbf{G}'')\cdot(\mathbf{G}-\mathbf{G}')\right]\left[\lambda_{\rm ex}(\mathbf{G}''-\mathbf{G}')\right]^2, \quad \text{(C3a)}$$

$$\mathbf{A}^{YX}_{\mathbf{G},\mathbf{G}'} = H\delta_{\mathbf{G},\mathbf{G}'} - 4\pi M_{\rm s}(\mathbf{G}-\mathbf{G}')\left[\chi(\mathbf{G}-\mathbf{G}')^2\frac{1-\zeta(\mathbf{G}-\mathbf{G}',d)}{|\mathbf{G}-\mathbf{G}'|^2} + \xi(\mathbf{G}',\mathbf{k})^2[\frac{\zeta(\mathbf{G}'+\mathbf{k},d)-1}{|\mathbf{G}'+\mathbf{k}|^2}])\right]$$
$$+ 4\pi\sum_{\mathbf{G}''} M_{\rm s}(\mathbf{G}-\mathbf{G}'')\left[(\mathbf{G}'+\mathbf{k})\cdot(\mathbf{G}''+\mathbf{k}) - (\mathbf{G}-\mathbf{G}'')\cdot(\mathbf{G}-\mathbf{G}')\right]\left[\lambda_{\rm ex}(\mathbf{G}''-\mathbf{G}')\right]^2. \quad \text{(C3b)}$$

Note that the one-dimensional case depicted in the paper, the Fourier coefficient of the saturation magnetization is

$$M_{\rm s}(G_n) = (M_{\rm s}-M'_{\rm s})\frac{w_z}{a_z}\mathrm{sinc}\left(G_n\frac{w_z}{2}\right) + M'_s\delta_{n,0}. \quad \text{(C4)}$$

The same structure was used for the exchange length coefficient, i.e.

$$\lambda_{\rm ex}(G_n) = (\lambda_{\rm ex}-\lambda'_{\rm ex})\frac{w_z}{a_z}\mathrm{sinc}\left(G_n\frac{w_z}{2}\right) + \lambda'_{\rm ex}\delta_{n,0}, \quad \text{(C5)}$$

where $\lambda'_{\rm ex}(\mathbf{r}) = 2A/4\pi M'_{\rm s}$.

[1] S. Demokritov and A. Slavin, *Magnonics: From Fundamentals to Applications*, Topics in Applied Physics (Springer Berlin Heidelberg, 2012).
[2] A. V. Chumak, V. I. Vasyuchka, A. A. Serga, and B. Hillebrands, Nat. Phys. **11**, 453 (2015).
[3] Y. Kajiwara, K. Harii, S. Takahashi, J. Ohe, K. Uchida, M. Mizuguchi, H. Umezawa, H. Kawai, K. Ando, K. Takanashi, S. Maekawa, and E. Saitoh, Nature **464**, 262 (2010).
[4] M. P. Kostylev, A. A. Serga, T. Schneider, B. Leven, and B. Hillebrands, Appl. Phys. Lett. **87**, 153501 (2005).
[5] S. Tacchi, P. Gruszecki, M. Madami, G. Carlotti, J. W. Kłos, M. Krawczyk, A. Adeyeye, and G. Gubbiotti, Sci. Rep. **5** (2015).
[6] A. Khitun and K. L. Wang, Superlattice. Microst. **38**, 184 (2005).
[7] A. Khitun, M. Bao, and K. L. Wang, J. Phys. D: Appl. Phys. **43**, 264005 (2010).
[8] M. Jamali, J. H. Kwon, S.-M. Seo, K.-J. Lee, and H. Yang, Sci. Rep. **3** (2013).
[9] J. O. Vasseur, L. Dobrzynski, B. Djafari-Rouhani, and H. Puszkarski, Phys. Rev. B **54**, 1043 (1996).
[10] S. Neusser, B. Botters, and D. Grundler, Phys. Rev. B **78**, 054406 (2008).
[11] S. Tacchi, F. Montoncello, M. Madami, G. Gubbiotti, G. Carlotti, L. Giovannini, R. Zivieri, F. Nizzoli, S. Jain, A. O. Adeyeye, and N. Singh, Phys. Rev. Lett. **107**, 127204 (2011).
[12] S. Tacchi, G. Duerr, J. W. Klos, M. Madami, S. Neusser, G. Gubbiotti, G. Carlotti, M. Krawczyk, and D. Grundler, Phys. Rev. Lett. **109**, 137202 (2012).
[13] Z. K. Wang, V. L. Zhang, H. S. Lim, S. C. Ng, M. H. Kuok, S. Jain, and A. O. Adeyeye, Appl. Phys. Lett. **94**, 083112 (2009).
[14] Z. K. Wang, V. L. Zhang, H. S. Lim, S. C. Ng, M. H. Kuok, S. Jain, and A. O. Adeyeye, ACS Nano **4**, 643 (2010).
[15] A. V. Chumak, V. I. Vasyuchka, A. A. Serga, M. P. Kostylev, V. S. Tiberkevich, and B. Hillebrands, Phys. Rev. Lett. **108**, 257207 (2012).
[16] H. Yu, G. Duerr, R. Huber, M. Bahr, T. Schwarze, F. Brandl, and D. Grundler, Nat. Commun. **4**, 2702 (2013).
[17] M. Krawczyk and D. Grundler, J. Phys.: Condens. Matter **26**, 123202 (2014).
[18] A. V. Chumak, A. A. Serga, and B. Hillebrands, Nat. Commun. **5**, 4700 (2014).
[19] S.-K. Kim, K.-S. Lee, and D.-S. Han, Appl. Phys. Lett. **95**, 082507 (2009).
[20] S. Nikitov, P. Tailhades, and C. Tsai, J. Magn. Magn. Mater. **236**, 320 (2001).
[21] M. K. H. Puszkarski, Solid State Phenom. **94**, 125 (2003).
[22] V. Kruglyak and R. Hicken, J. Magn. Magn. Mater. **306**, 191 (2006).
[23] G. Gubbiotti, S. Tacchi, G. Carlotti, N. Singh, S. Goolaup, A. O. Adeyeye, and M. Kostylev, Appl. Phys. Lett. **90**, 092503 (2007).
[24] M. Krawczyk and H. Puszkarski, Phys. Rev. B **77**, 054437 (2008).
[25] A. V. Chumak, P. Pirro, A. A. Serga, M. P. Kostylev, R. L. Stamps, H. Schultheiss, K. Vogt, S. J. Hermsdoerfer, B. Laegel, P. A. Beck, and B. Hillebrands, Appl. Phys. Lett. **95**, 262508 (2009).
[26] S. Neusser and D. Grundler, Adv. Mater. **21**, 2927 (2009).
[27] A. A. Serga, A. V. Chumak, and B. Hillebrands, J. Phys. D: Appl. Phys. **43**, 264002 (2010).
[28] V. V. Kruglyak, S. O. Demokritov, and D. Grundler, J. Phys. D: Appl. Phys. **43**, 264001 (2010).
[29] G. Gubbiotti, S. Tacchi, M. Madami, G. Carlotti, A. O. Adeyeye, and M. Kostylev, J. Phys. D: Appl. Phys. **43**, 264003 (2010).
[30] Y. Cao, G. Yun, X. Liang, and N. Bai, J. Phys. D: Appl. Phys. **43**, 305005 (2010).
[31] B. Lenk, H. Ulrichs, F. Garbs, and M. Münzenberg, Phys. Rep. **507**, 107 (2011).
[32] K.-S. Lee, D.-S. Han, and S.-K. Kim, Phys. Rev. Lett. **102**, 127202 (2009).

[33] J. Ding, M. Kostylev, and A. O. Adeyeye, Phys. Rev. B **84**, 054425 (2011).

[34] T. Sebastian, K. Schultheiss, B. Obry, B. Hillebrands, and H. Schultheiss, Front. Phys. **3**, 35 (2015).

[35] J. W. Kłos, D. Kumar, J. Romero-Vivas, H. Fangohr, M. Franchin, M. Krawczyk, and A. Barman, Phys. Rev. B **86**, 184433 (2012).

[36] M. Krawczyk, S. Mamica, M. Mruczkiewicz, J. W. Klos, S. Tacchi, M. Madami, G. Gubbiotti, G. Duerr, and D. Grundler, J. Phys. D: Appl. Phys. **46**, 495003 (2013).

[37] P. Landeros and D. L. Mills, Phys. Rev. B **85**, 054424 (2012).

[38] M. Körner, K. Lenz, R. A. Gallardo, M. Fritzsche, A. Mücklich, S. Facsko, J. Lindner, P. Landeros, and J. Fassbender, Phys. Rev. B **88**, 054405 (2013).

[39] S. A. Odintsov, A. V. Sadovnikov, A. A. Grachev, E. N. Beginin, Y. P. Sharaevskii, and S. A. Nikitov, JETP Letters **104**, 563 (2016).

[40] M. Langer, F. Röder, R. A. Gallardo, T. Schneider, S. Stienen, C. Gatel, R. Hübner, L. Bischoff, K. Lenz, J. Lindner, P. Landeros, and J. Fassbender, Phys. Rev. B **95**, 184405 (2017).

[41] I. Barsukov, F. M. Römer, R. Meckenstock, K. Lenz, J. Lindner, S. Hemken to Krax, A. Banholzer, M. Körner, J. Grebing, J. Fassbender, and M. Farle, Phys. Rev. B **84**, 140410 (2011).

[42] B. Obry, P. Pirro, T. Brächer, A. V. Chumak, J. Osten, F. Ciubotaru, A. A. Serga, J. Fassbender, and B. Hillebrands, Appl. Phys. Lett. **102**, 202403 (2013).

[43] R. A. Gallardo, A. Banholzer, K. Wagner, M. Körner, K. Lenz, M. Farle, J. Lindner, J. Fassbender, and P. Landeros, New J. Phys. **16**, 023015 (2014).

[44] Q. Wang, A. V. Chumak, L. Jin, H. Zhang, B. Hillebrands, and Z. Zhong, Phys. Rev. B **95**, 134433 (2017).

[45] C. S. Lin, H. S. Lim, Z. K. Wang, S. C. Ng, and M. H. Kuok, Appl. Phys. Lett. **98**, 022504 (2011).

[46] M. Sokolovskyy and M. Krawczyk, J. Nanopart. Res. **13**, 6085 (2011).

[47] M. Mruczkiewicz, M. Krawczyk, V. K. Sakharov, Y. V. Khivintsev, Y. A. Filimonov, and S. A. Nikitov, J. Appl. Phys. **113**, 093908 (2013).

[48] A. Vansteenkiste, J. Leliaert, M. Dvornik, M. Helsen, F. Garcia-Sanchez, and B. Van Waeyenberge, AIP Adv. **4**, 107133 (2014).

[49] K. Wagner, S. Stienen, and M. Farle, arXiv:1506.05292 (2015).

[50] R. D. McMichael and M. D. Stiles, J. Appl. Phys. **97**, 10J901 (2005).

[51] O. Gladii, M. Haidar, Y. Henry, M. Kostylev, and M. Bailleul, Phys. Rev. B **93**, 054430 (2016).

[52] K. Di, S. X. Feng, S. N. Piramanayagam, V. L. Zhang, H. S. Lim, S. C. Ng, and M. H. Kuok, Sci. Rep. **5**, 10153 EP (2015).

[53] K. Zakeri, Y. Zhang, J. Prokop, T.-H. Chuang, N. Sakr, W. X. Tang, and J. Kirschner, Phys. Rev. Lett. **104**, 137203 (2010).

[54] D. Cortés-Ortuño and P. Landeros, J. Phys.: Condens. Matter **25**, 156001 (2013).

[55] K. Di, V. L. Zhang, H. S. Lim, S. C. Ng, M. H. Kuok, J. Yu, J. Yoon, X. Qiu, and H. Yang, Phys. Rev. Lett. **114**, 047201 (2015).

[56] J. Cho, N.-H. Kim, S. Lee, J.-S. Kim, R. Lavrijsen, A. Solignac, Y. Yin, D.-S. Han, N. J. J. van Hoof, H. J. M. Swagten, B. Koopmans, and C.-Y. You, Nat. Commun. **6** (2015).

[57] H. T. Nembach, J. M. Shaw, M. Weiler, E. Jue, and T. J. Silva, Nat. Phys. **11**, 825 (2015).

[58] S. Tacchi, R. E. Troncoso, M. Ahlberg, G. Gubbiotti, M. Madami, J. Åkerman, and P. Landeros, Phys. Rev. Lett. **118**, 147201 (2017).